Enhancing of corrosion protection properties of stainless steel 316L using chemically synthesized thin film poly(pyrrole-co-*p*-toluidine) coating on SS316L surface in a 3.5 wt.% NaCl medium

S.A. Lasaddy,[1] A.M. Farhan[2]* and A.A. Jabor[3]

[1]*Department of Chemistry, College of Science, University of Baghdad, Jadriya,10011 Baghdad, Iraq*
[2]*Department of Chemistry, College of Science for Women, University of Baghdad, Jadriya, 10011 Baghdad, Iraq*
[3]*Ministry of Higher Education and Scientific Research, Jadriya, Baghdad, Iraq*
**E-mail: af8832@gmail.com*

Abstract

Conducting polymers have garnered attention due to their economic feasibility and numerous industrial applications. Polymers possess long-chain carbon bonds that prevent a significant number of metal surfaces from disintegrating when they adsorb them. A barrier between the metal and its surroundings is established by the thin layers that have been adsorbed onto the metal substrate. A coating of thin film poly(pyrrole-co-*p*-toluidine) was made on stainless steel 316L to protect it better. This was done by chemical oxidative copolymerization with ammonium persulfate as an oxidant in hydrochloric acid water. The chemical structure of the obtained copolymer is characterized by Fourier Transform Infrared Spectroscopy (FTIR) techniques. The copolymer was characterized using XRD, EDS, and the 3-dimensional morphology of the coatings as determined by atomic force microscopy (AFM). To evaluate the protection performance of deposited coatings, their open circuit potential (OCP) values were monitored using a linear polarization process. The corrosion protection efficiency of thin film poly(pyrrole-co-*p*-toluidine) was assessed through electrochemical measurements of corrosion potential (E_{corr}), polarization resistance (R_p), corrosion current density (i_{corr}), and Tafel extrapolation methods in a 3.5 wt.% NaCl medium. The copolymer coatings' surface morphology was investigated using field emission scanning electron microscopy (FESEM). The results indicate that poly(pyrrole-co-*p*-toluidine) coating is a potential coating material for preventing corrosion of SS316L in the corrosive medium mentioned above. We determined the protection efficiency by varying the temperature between 298 and 328 K in the absence and presence of (pyrrole/*p*-toluidine) copolymer coating and computed the values E_a, ΔS^0, ΔH^0, and ΔG^0.

Received: January 25, 2025 Published: March 5, 2025 doi: 10.17675/2305-6894-2025-14-1-14

Keywords: *corrosion, conducting polymer, electrochemical technique, pyrrole, p-toluidine.*

1. Introduction

The metallic component is susceptible to damage due to corrosion, which presents a substantial challenge. This can lead to environmental hazards and economic losses for Mother Nature. The continuous and detrimental nature of corrosion presents a challenge to the entire globe. The complete eradication would be impractical and unattainable; however, prevention is more effective and practicable. To resolve this matter, an anti-corrosive thin film coating is applied to the metal surface [1]. The conjugated (or conducting) polymers (CPs) are materials that exhibit exceptional anti-corrosion properties. In the past ten years, some CPs were looked at as possible replacements for chromium-containing materials that are bad for your health and the environment as anti-corrosion coatings. One important thing about a CP coating, when it is conductive, is that it can store a lot of charge at the point where it meets a metal's passive layer. It is possible to oxidize base metal with this charge and create a passive layer; Consequently, a CP works as a barrier [2]. In the past 25 years, researchers made a lot of progress in understanding and using conducting and electroactive conjugated polymers. These polymers can now be found in many technological fields and are used in things like solar cells, anticorrosion coatings, sensors, and biosensors [3–5]. Before the discovery of polyacetylene (PA) approximately forty years ago, it was unimaginable that organic polymers could serve as electrical conductors on a par with metals. This is because polymers have been consistently regarded as insulators. During the 1970s, the notion that the electrically conductive properties of conjugated organic polymers could be modified through doping was challenged by polymer chemist Hideki Shirakawa, physicist Alan J. Heeger, and inorganic chemist Alan G. MacDiarmid [6–12]. As they observed, the electrical conductivity of a thin film of Polyaniline increased by a billion times when it was polarized by iodine vapors [7]. In recognition of this remarkable discovery, they received the 2000 Nobel Prize in Chemistry for their contributions to the development of conducting polymers. Intrinsically Conducting Polymers (ICPs), also referred to as synthetic metals, are organic polymers that have the electrical and optical characteristics of metal while still having the mechanical, processable, and other characteristics of conventional polymers. Figure 1 illustrates the chemical structure of specific conjugated polymers form, which depicts their neutral insulating state [13].

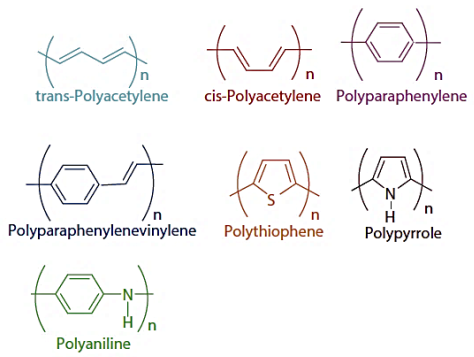

Figure 1. Examples of the more common conjugated polymers in their neutral form.

Figure 2 represents the most commonly accepted mechanism of polyacetylene, which is based on its high electrical conductivity and simple chemical structure. Because they are conjugated, polymers naturally have single and double bonds that can change places through the polymer backbone. These single and double bonds contain a localized σ-bond, which is recognized may be involved in some mechanism for the establishment of a robust chemical bond, metals and alloys are mainly based on the metallic bond, additionally, it is acknowledged that every double bond contains a delocalized π-bond, which is weaker than the σ-bond [14, 15]. This chain of conjugated π-bonds exhibits an overlap of the p_z-orbital, which enable the π-electrons to readily traverse the carbon backbone. An anticorrosion organic coating operates on the following principle. An active corrosion cell necessitates the presence of an oxidant at the metal surface and a mechanism for ion movement along the surface between the anodic and cathodic sites to maintain charge balance. The coatings lower the rate of corrosion by slowing the mobility of ions on the coating surface and the pace at which ionic species (such as H^+ ions and water) may reach the metal/coating interface. Thus, it raises the ohmic of the corrosion cell becoming polarized. Fundamentally, the anticorrosion coating functions as a protective layer between the metal and its surroundings [16]. Conducting polymers have been used for anti-corrosion. A dual protection mechanism is demonstrated by this conducting polymer, which shifts the potential of the underlying metal into the passive region and provides anodic protection. The second function is to serve as a protective barrier against exceedingly corrosive conditions [17].

This study has used a chemical polymerization process to make conducting copolymer films on SS316L. Then we tested the films' ability to protect against corrosion in a 3.5% NaCl solution at temperatures between 298 and 328 K.

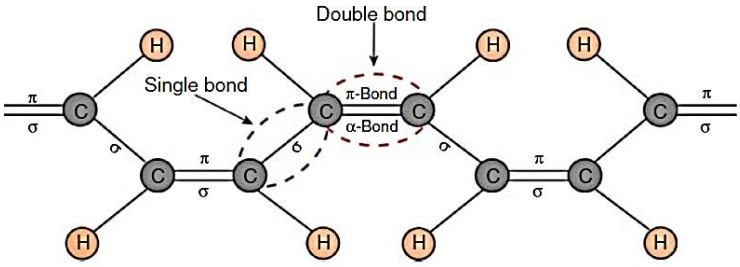

Figure 2. Scheme describing the conjugated π-system in *cis*-polyacetylene.

2. Experimental Procedures

2.1. Materials

The pure pyrrole precipitation procedure has been used by applying 98% Aldrich monomer. Chemicals provided the ammonium persulfate (APS, 99.9%) and para-toluidine C_7H_9N. Additionally, BDH was used to supply ethanol (99% C_2H_5OH) and 36% hydrochloric acid (HCl). Aqueous solutions were prepared using twice-distilled water.

2.2. Preparation of specimens

This study has used 316L stainless steel as the substrate, measuring 2.5 cm in area and 2.0 mm in thickness. The chemical composition of the stainless-steel substrate is presented in Table 1. To make the samples smooth, #80, #400, #600, #800, #1000, #1200, #1500, and #2000 grit SiC (silicon carbide) abrasive paper to achieve a smooth surface. before the experiments. We then thoroughly degreased the specimens with acetone to eliminate any remaining contaminants.

Table 1. Chemical composition of the 316L stainless steel.

Material	**Cu%**	**Ni%**	**Si%**	**Mn%**	**P%**	**S%**	**Cr%**
SS316L	0.213	11.07	0.055	1.066	0.0016	0.018	15.97
Material	**Mo%**	**Al%**	**Ti%**	**Mg%**	**Zn%**	**Fe%**	**Mo%**
SS316L	1.278	0.0086	0.0028	0.037	0.0057	Balance	1.278

2.3. Chemical synthesis of poly(pyrrole-co-p-toluidine)

Chemical oxidative polymerization is an extensively used method for the fabrication of CP-based coatings due to its ease of use in the production of CPs on a large scale. This is necessary, for instance, it is essential to safeguard large metal surfaces. The chemical oxidative copolymerization method previously described [18, 19, 20] was employed to synthesize poly(pyrrole-co-*p*-toluidine) copolymer. A typical method for synthesizing copolymers with a 50:50 monomer ratio. In the subsequent step, the monomer solution was subjected to the oxidant solution, which was added dropwise at a rate of 1 drop every 3 seconds for approximately 1 hour (the monomer/oxidant total molar ratio = 1/1). The reaction solution immediately underwent a blue-violet hue following the addition of the initial few droplets. The magnetic stirrer was utilized to perpetually agitate the mixture for 24 hours. The copolymer hydrochloride salt was cleared of oxidants and oligomers through filtration and subsequent rinsing with an excessive amount of distilled water. The mixture was then desiccated in an oven at 60°C for 24 hours. During the polymerization, within fifteen to 20 min (after reactants were mixed) it is noticed a color shift pattern from yellow to light green, followed by a Greenish-black product precipitate. This dark green color product is called poly(pyrrole-co-*p*-toluidine). A glass slide (2.5×2 cm) was placed in the beaker to deposit the formed copolymer onto the glass. The glass slides were washed with water and ethanol and dried in an oven at 50°C for 5 minutes. The structure of synthesized copolymer film was given in the following reaction scheme:

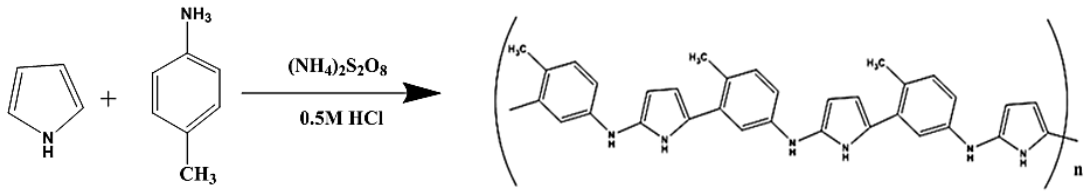

Reaction scheme

2.4. Fourier transform infrared (FTIR) spectroscopy analysis

Using a 1 cm^{-1} resolution, the Fourier Transform Infrared spectra of the granules were recorded in the KBr medium at room temperature, with an average of 15 images, and the Fourier transform infrared (FTIR) spectra of the samples were obtained using a Shimadzu 8101 M spectrophotometer in the wave number range 400 to 4000 cm^{-1}. FTIR studies were carried out to confirm the polymerization of the monomer throughout the synthesis procedure and the existence of functional groups in the resulting copolymer.

2.5 Differential scanning calorimetry (DSC)

Thermo-analytical techniques, such as DSC, are used to ascertain the heat and temperature flux associated with a sample according to temperature and time.

A DSC-50, which was manufactured by Shimadzu in Japan, was employed to conduct DSC measurements. The initial temperature was 25°C, which was incrementally increased by 10°C every minute until it reached 300°C. Subsequently, it was chilled to room temperature.

2.6. X-Ray diffraction (XRD)

Cu-Kα (1.5418 Å) radiation was employed to conduct X-ray diffraction (XRD) experiments using a 30 kV, Model PW3040/60, 20 mA PAN Analytical Rontgen Diffractometer System, Netherlands. The step width was 0.02°, and the step time was 1.25 seconds, and the XRD patterns were recorded in the 2θ range of 10 to 70°.

2.7. Atomic force microscopy AFM

Surface roughness and particle sizes of prepared or synthesized materials were analyzed using atomic force microscopy (*Core AFM 2023 model, manufactured by Nano surf AG, Switzerland*).

All measurements were conducted at the general service lab in the Chemistry department, College of Sciences at the University of Baghdad.

2.8. Field emission scanning electron microscopy (FESEM)

The surface morphology and element composition of poly(pyrrole-co-*p*-toluidine) copolymer were analyzed by A field emission scanning electron microscope (FESEM, Inspect ^{TM} F50 DS0019) fitted with an EDS (energy dispersive spectrometer).

2.9. Potentiodynamic polarization measurements

We conducted all electrochemical measurements using the Princeton Applied Research PAR2273 Potentiostat/Galvanostat. We used a potentiostatic setup to measure electrochemical parameters. This included the host computer, thermostat, the magnetic stirrer, and the M lab potentiostat-galvanostat. The medium was a 3.5 wt.% NaCl solution that was maintained at varying temperatures. There are three electrodes in the corrosion cell. The working electrodes have been fabricated in the form of circular discs with an apparent surface area of 1 cm^2 while the counter electrode is a Pt wire. The reference electrode is a saturated calomel electrode positioned near the surface working electrode. Then the test solution was poured into the corrosion cell. The open circuit potential (OCP), which describes the behavior of the metal, was calculated using the steady-state potential. Then, the applied voltage on the working electrode was established to shift the cathodic direction to the anodic direction to record the polarization curves. The potentiostatic setup is illustrated in Figure 3.

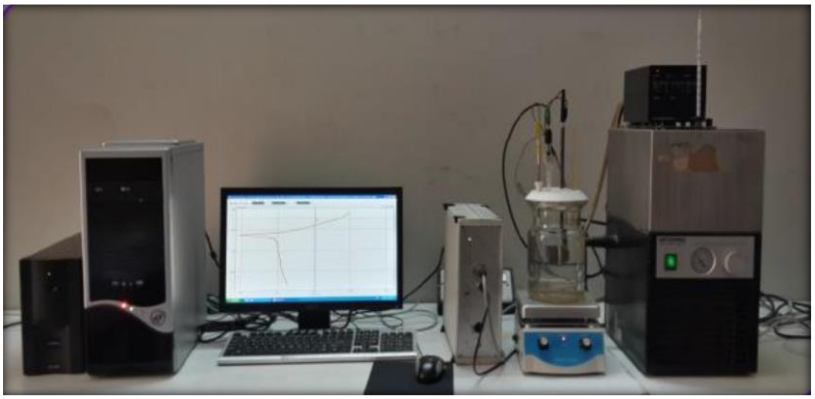

Figure 3. The three-electrode corrosion cell.

3. Results and Discussion

3.1. Electrochemical studies of the coating

3.1.1. Measurement of open circuit potential (OCP) vs. time

To determine the open circuit potential (OCP) of the specimen corrosion, samples were submerged in a solution of saline water with (3.5%) NaCl with exposure to various temperatures (25, 35, 45, and 55) °C in order to accomplish the steady state between the

sample and electrolytic solution. The contrast in the potential based on the current has been recorded as a time step for every specimen. When the steady state condition is achieved, the determined potential is known as open circuit potential. After determining the OCP, low current from cathodic current passes through the specimens by reducing the magnitude of variable resistance gradually. Then the working electrode potential is measured against the current by a potentiostatic device to determine the value of current density.

3.1.2. Electrochemical polarization measurements

Polarization methods entail the modification of the WE's potential and the monitoring of the current generated as a function of time or potential. One of the most essential physical quantities that DC polarization methods measure is linear polarization resistance (LPR).

During LPR measurements, the electrochemical response of a corroding metal is analyzed at its open circuit potential, which is equivalent to the corrosion potential. The equation determines the net current density that passes through a corroding metal–electrolyte interface:

$$i = i_{\text{corr}}\left[\exp\left\{\frac{2.303(E-E_{\text{corr}})}{\beta_{\text{a}}}\right\}\right]-\left[\exp\left\{-\frac{2.303(E-E_{\text{corr}})}{\beta_{\text{c}}}\right\}\right]$$

where i denotes the net current density that passes through the interface between the metal and electrolyte in unit of A/cm^2; i_{corr} is the corrosion current density (A/cm^2); E_{corr} and E represent the corrosion potential (V) and the measured potential (V), (β_a); and (β_c) are Tafel slopes (V/decade) [21]. In the temperature range of 25–55 C°, potentiodynamic polarization investigations were conducted, as illustrated in Figure 4.

The parameters extracted from potentiodynamic polarization (PDP) measurements, including potential (E_{corr}), i_{corr} corrosion, and %η with and without inhibitor, are recorded in Table 2.

The corrosion rate should be calculated by converting the corrosion current values derived from the Tafel extrapolation and polarization resistance approaches. For this reason, it is reasonable to presume that the current distribution is consistent throughout the area utilized in the calculation. This assumption leads to the division of the current value by the surface area, as illustrated in (Equation 1).

$$i_{\text{corr}} = \frac{i}{A} \tag{1}$$

where i_{corr} is the current density (μA/cm^2), i is the current (μA), and A is the exposed specimen area, cm^2. Based on Faraday's law, the corrosion rate (CR) (Equation 2) can be calculated as:

$$CR = K_1\left(\frac{i_{\text{corr}}}{d}\right)EW \tag{2}$$

where *CR* is expressed in millimeters per year, i_{corr} is expressed in μA/cm^2, and K_1 is $3.27 \cdot 10^{-3}$ in milligrams per cubic centimeter per year, *EW* is the equivalent weight, *d* is the density in grams per cubic centimeter and the *EW* of pure elements is calculated as (Equation 3):

$$EW = \frac{W}{n} \tag{3}$$

where *W* is the atomic weight of the element and *n* is the number of electrons required to oxidize an atom of the element in the corrosion process.

The Stern-Geary equation (Equation 4) was employed to determine the polarization resistance (R_p) values [22]. b_c and b_a are cathodic and anodic Tafel slopes, respectively. Potentiodynamic polarization investigations were achieved for SS316L Uncoated and coated with Copolymer after immersion in NaCl 3.5% for 20 min within the temperature range of 25–55°C.

$$R_p = \frac{b_a \cdot b_c}{2.303 \cdot i_{corr}\left(b_a + b_c\right)} \tag{4}$$

A defined surface with an area of 2.5 cm^2 was exposed to the solution. Table 2 provides the values of the corresponding protection efficiencies (η%), anodic and cathodic Tafel slopes (b_a, b_c), polarization resistance (R_p) values, and corrosion potential (E_{corr}) associated electrochemical parameters. These values were calculated from Tafel plots and illustrated in Figure 4.

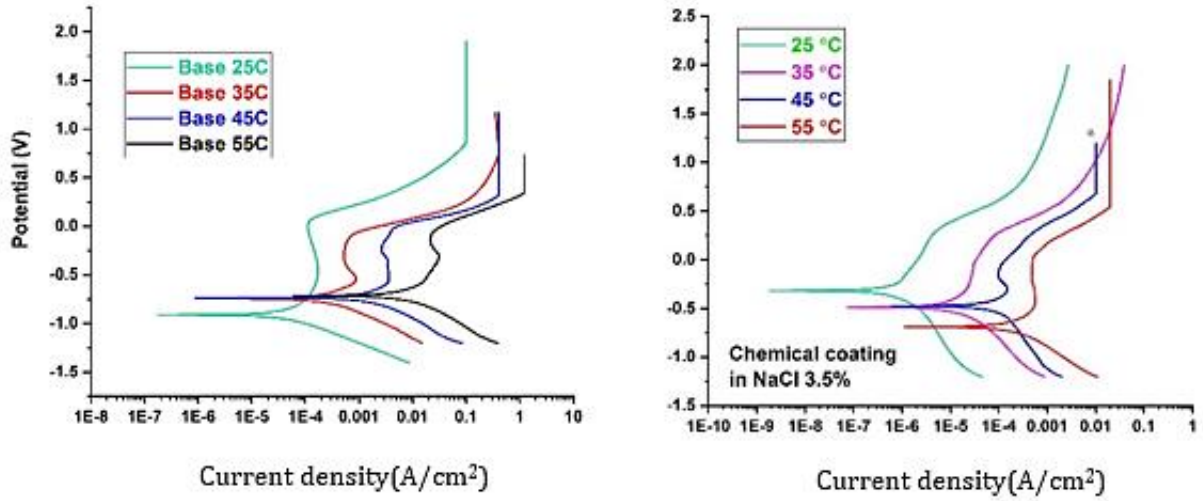

Figure 4. Polarization curves of stainless steel 316L for uncoated and coated with poly(pyrrole-co-*p*-toluidine) at different temperatures in 3.5 wt.% NaCl.

Table 2. Corrosion parameter of for Uncoated and coated with Poly(pyrrole-co-*p*-toluidine) at different temperatures in 3.5 wt.% NaCl.

ITEM	T, K	E_{corr}, V	i_{corr}, A/cm^2	Corr. rate, mmpy	$-b_c$, V·dec^{-1}	b_a, V·dec^{-1}	OCP, V	R_p, Ω·cm^2	Protection efficiency, %
Uncoated	298	–0.911	$1.47\cdot10^{-5}$	$1.62\cdot10^{-1}$	0.156	0.232	–0.411	3148	
	308	–0.733	$7.98\cdot10^{-5}$	$8.22\cdot10^{-1}$	0.170	0.214	–0.462	515	
	318	–0.741	$5.01\cdot10^{-4}$	5.53	0.172	0.242	–0.486	87.2	
	328	–0.707	0.002	23.3	0.183	0.259	–0.493	23.3	
Coated	298	0.316	$2.90\cdot10^{-7}$	$2.90\cdot10^{-2}$	0.265	0.343	–0.050	227000	98%
	308	–0.493	$2.02\cdot10^{-6}$	$2.24\cdot10^{-2}$	0.177	0.299	–0.189	23828	97%
	318	–0.483	$1.90\cdot10^{-5}$	$2.10\cdot10^{-2}$	0.251	0.290	–0.217	3084	96%
	328	–0.699	$4.16\cdot10^{-5}$	$4.59\cdot10^{-1}$	0.176	0.223	–0.222	1031	97.9%

Table 2 indicates that the protective action of poly(pyrrole-co-*p*-toluidine) on SS316L results in a shift in E_{corr} to more positive values (Figure 4), as compared to the uncoated electrode. This is due to the inhibition of redox reactions that occur at the interface between the metal and the electrolyte.

The curvature's shift at a lower current density suggests that the corrosion process was delayed by the molecules' adsorption on the metal surface. According to Santos et al., the corrosion current density values for coated steel transited towards a lower current density, which is due to the oxidation of the bilayer coating rather than the corrosion of the substrate alloy [23]. The interface's protection against O_2 and H^+ reduction is enhanced by the increase in R_p. The copolymer's inhibitive property is primarily attributed to the coexistence of quaternary nitrogen atoms with numerous π-electron clouds.

The extended molecular size obstructs the reaction sites, resulting in a reduction of the effective area for corrosion reaction and increased adsorption on the stainless-steel surface [24]. An uncoated medium exhibits a higher rate of corrosion than one that has been coated. When the temperature rises, the rate of corrosion increases because the heated movement of inhibitor molecules weakens the steel surfaces' adsorption ability, which causes the corrosion process to proceed more quickly [25].

It is clear from the resulting data that the corrosion potential (E_{corr}) and the corrosion current density (i_{corr}) were increased with the increase in temperature. E_{corr} was shifted to more active values (cathodic) with rising temperatures. Furthermore, the Tafel plots showed that in contrast to the blank S.S., the E_{corr} for the coated S.S. was moved into a higher location (noble direction). This suggests that corrosion prevention serves as anodic protection [26]. However, in both the inhibitor's presence and absence, the inhibitor's inhibition decreases as the temperature rises.

3.1.3. Corrosion kinetics and thermodynamics

Studying thermodynamic properties determines the mechanism of the adsorption process that contributes to corrosion. The thermodynamic parameters, such as entropy (ΔS^0) and enthalpy (ΔH^0), were computed using the transition state theory equation (Equation 5) of the corrosion process in the absence and presence of a coated in a 3.5 wt.% NaCl environment [27, 28].

$$\log\left(\frac{C_R}{T}\right)=\left[\log\left(\frac{R}{Nh}\right)+\frac{\Delta S^0}{2.303RT}\right]-\frac{\Delta H^0}{2.303RT} \quad (3)$$

In this equation, N is Avogadro's number ($6.022\cdot10^{23}$ mol^{-1}), R is the universal gas constant 8.314 J/kmol), T is the medium temperature, and h is Planck's constant (6.62617610^{-34} J·s). The linearity of the $\log(i_{corr}/T)$ plot against $1/T$ is illustrated in Figure 5. The slopes and intercept of the graph were used to derive the values (ΔH^0) and (ΔS^0), which are illustrated in Table 3.

Table 3. Corrosion kinetic parameters at different temperatures for uncoated SS316L and coated with poly(pyrrole-co-*p*-toluidine) in 3.5 wt.% NaCl.

T, K	$1/T$, K^{-1}	i_{corr}, A/cm^2	log i_{corr}	log i_{corr}/T	ΔG^0, kJ/mol	ΔH^0, kJ/mol	ΔS^0, J·kJ/mol	E_a, kJ/mol	A, molecules, cm^{-2}·s^{-1}
Uncoated									
298	0.0033	$1.47\cdot10^{-5}$	–4.83	–7.31	103	135	109	363	$5.42\cdot10^{42}$
308	0.0032	$7.98\cdot10^{-5}$	–4.09	–6.58	102				
318	0.0031	$5.01\cdot10^{-4}$	–3.30	–5.80	101				
328	0.0030	0.002	–2.69	–5.21	99				
Coated									
298	0.0033	$2.90\cdot10^{-7}$	–6.53	–9.01	112	139	92.9	347	$1.49\cdot10^{38}$
308	0.0032	$2.02\cdot10^{-6}$	–5.69	–8.18	111				
318	0.0031	$1.90\cdot10^{-5}$	–4.72	–7.23	110				
328	0.0030	$4.15\cdot10^{-5}$	–4.38	–6.89	109				

The Arrhenius equation, as presented in (Equation 6), was employed to ascertain the activation energy E_a in the absence and presence of copolymer.

$$\log C_R=\log A-\frac{E_a}{2.303RT} \quad (6)$$

where A is the frequency factor, T is the absolute temperature, R is the universal gas constant, E_a is the apparent activation energy, and CR is the rate of corrosion.

Based on the Arrhenius plot of log i_{corr} against the reciprocal of absolute temperature ($1/T$) in Figure 6, which produces a straight line with a slope of $-E_a/2.303R$, the activation energy of the corrosion process was computed and reported in Table 3.

Equation 6 of the transition state theory was used to determine the enthalpy of activation (ΔH^*) and the entropy of activation (ΔS^*) for mild steel corrosion in 3.5 NaCl.

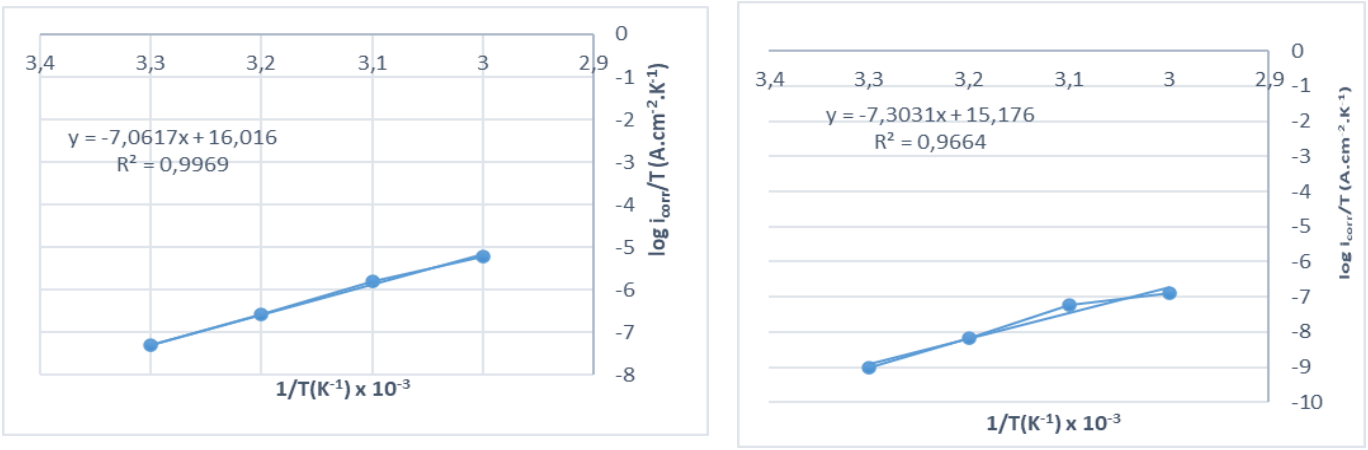

Figure 5. Arrhenius plots of log i_{corr}/T *vs.* $1/T$ of stainless steel 316L for uncoated (left) and coated with poly(pyrrole-co-*p*-toluidine) (right) in 3.5% NaCl at different temperatures.

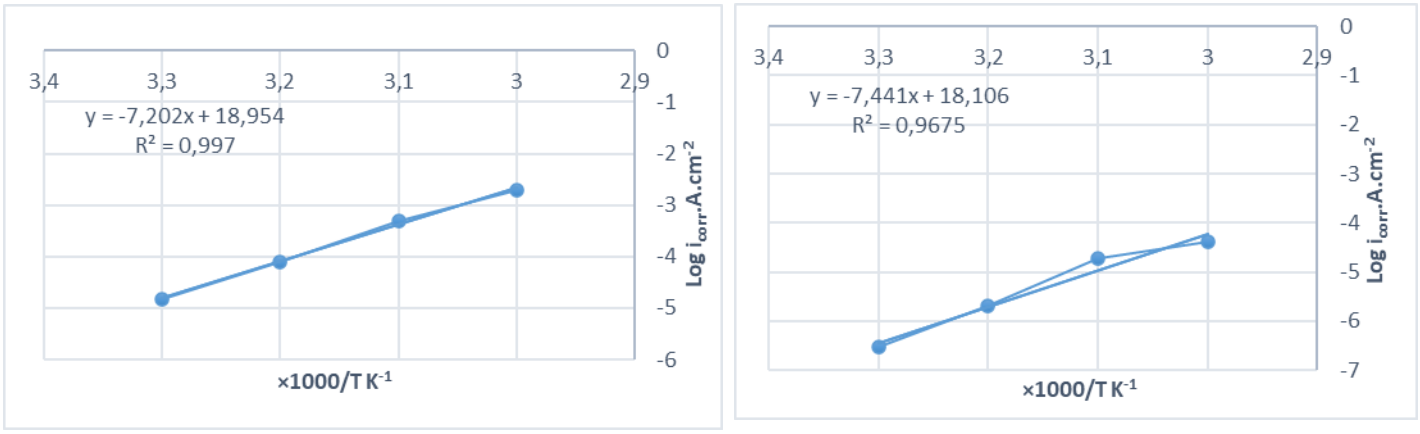

Figure 6. Arrhenius plot of log i_{corr} *vs.* $1/T$ for corrosion of stainless steel 316L for uncoated (left) and coated with poly(pyrrole-co-*p*-toluidine) (right) in 3.5% NaCl at different temperatures.

The positive values of the enthalpy of activation (ΔH^0) prove that the process of desorption of the inhibitor on the stainless-steel surface is endothermic. The entropy of activation (ΔS^0) values is positive, indicating that the inhibitor's adsorption on the stainless-steel surface is driven by an increase in entropy that occurs throughout the adsorption process [29].

According to Riggs and Hurd [30], a shift in the net corrosion reaction from the exposed to the covered sections of the metal surface may be the cause of the E_a drop when an inhibitor is present.

Table 3 shows that the decrease of the ΔG^0 with an increase in temperature indicates that the adsorption of inhibitor on the surface of stainless steel was adverse at high temperatures.

3.2. Thermal stability results

3.2.1. Differential scanning calorimetry (DSC) results

Thermal degradation behaviors of copolymer poly(pyrrole-co-*p*-toluidine) were investigated by differential scanning calorimetry (DSC). The graphs of temperature (°C) versus heat flow (*W*/*g*) are shown in Figure 7. The copolymer structure's removal of moisture is the cause of the minimal weight loss seen at temperatures between 120 and 140°C [31]. The chemically synthesized copolymer shows two-step weight loss, the first weight loss (130.47°C) indicates removing dopant anions from the polymer structure while the second weight loss (240.80°C) for the chemically synthesized copolymer is associated with the heat breakdown of the polymer chains.

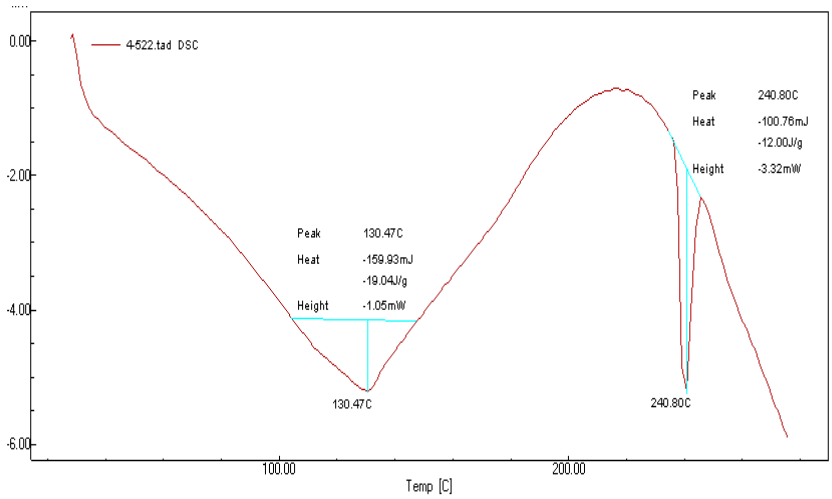

Figure 7. Differential scanning calorimetry analysis for poly(pyrrole-co-*p*-toluidine).

3.3. Fourier transform infrared (FT-IR) spectrometry

Figure 12 shows the FTIR spectrum of poly(pPY-co-*p*-toluidine), and the FT-IR band observed at 3470 cm^{-1} has been designated to N–H stretching modes of vibrations in *p*-toluidine and pyrrole units [36].

The aromatic and aliphatic C–H stretching vibrations should be attributed to the bands at approximately 3292, 3257, 3245, and 3215 cm^{-1}, respectively [37].

The bands at around 808–892 and 939 cm^{-1} correspond to C–H out-of-the-plane and C–H in-plane deformation vibrations respectively for polypyrrole 1573 cm^{-1} and 1583 cm^{-1} for C=C stretching for *p*-toluidine. A strong absorption band was observed at 1625 cm^{-1} for C=C stretching for pyrrole.

The weak absorption band at 1400 cm^{-1} was observed due to the deformation vibration of the methylene group. The band observed at 1342 cm^{-1} of the title compound is assigned to C–N stretching modes of vibration. The FT-IR band observed at 1519 cm^{-1} of the title compound is assigned to C–C stretching for *p*-toluidine [38]. The band observed at 1056 cm^{-1} is assigned to S=O stretching vibrations from APS [39].

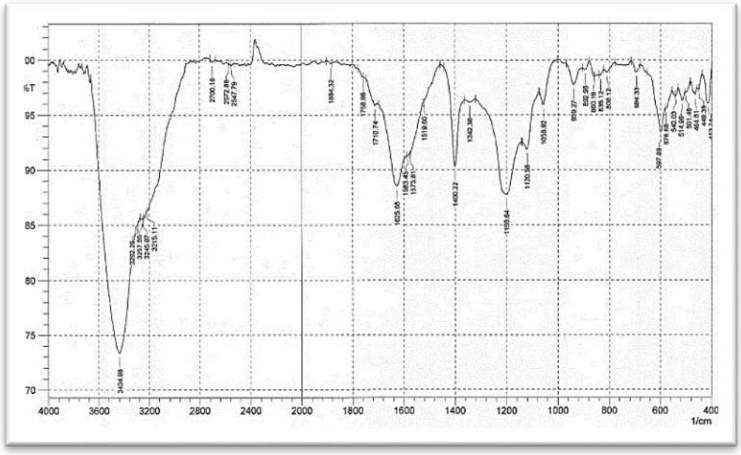

Figure 12. FT-IR spectra of poly(pyrrole-co-*p*-toluidine) copolymer coating.

3.4. Chemical composition analysis and surface elemental by EDS

The EDS analyses of the ternary Poly(pyrrole-co-*p*-toluidine), as shown in Figure 8 confirm the presence of peaks attributed to C, N, O, Cl, and S, thus proving the existence of poly(pyrrole-co-*p*-toluidine) in the system and the percent of ions as shown in Table 3.

Table 3. EDS measurement for poly(pyrrole-co-*p*-toluidine) coating on SS316L.

Element	Weight, %	Atomic, %
C	39.6	48.3
N	13.4	14.1
O	35.3	32.4
S	8.9	4.1
Cl	2.8	1.2

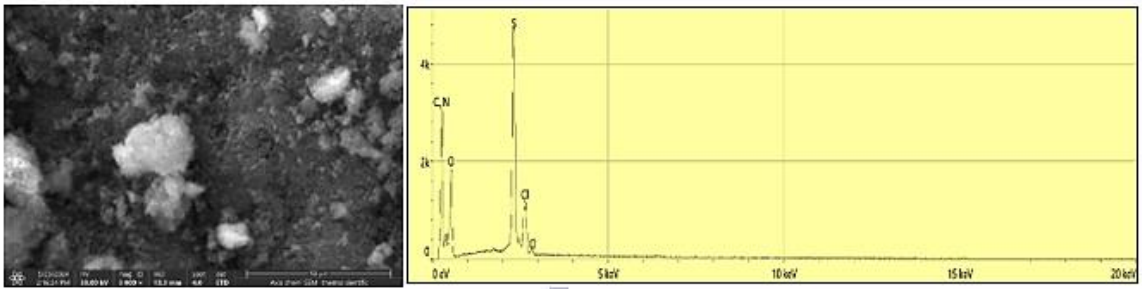

Figure 8. EDS spectra for poly(pyrrole-co-*p*-toluidine) coating on SS316L.

3.5. Atomic force microscopy

AFM was used to determine the coating's surface morphology and roughness. The surface morphology of a protective substrate coated with a polymer film layer plays a great role in enhancing corrosion protection efficiency. AFM images showed the morphology of the surface of the poly(pyrrole-co-*p*-toluidine) to be a homogeneous exterior with spherical particles of regular size as well as uniform distribution. The most often utilized parameter in AFM analysis to describe the surface roughness of polymer films is Root Mean Square Roughness (RMS). AFM images show morphology of copolymer film during polymerization on SS316L has a surface roughness (11.19 nm) with an average diameter of around (68.92 nm). The three-dimensional structure of SS316L coated with poly(pyrrole-co-*p*-toluidine) together with the average diameter and Root Mean Square Roughness (RMS) is shown in Figure 9.

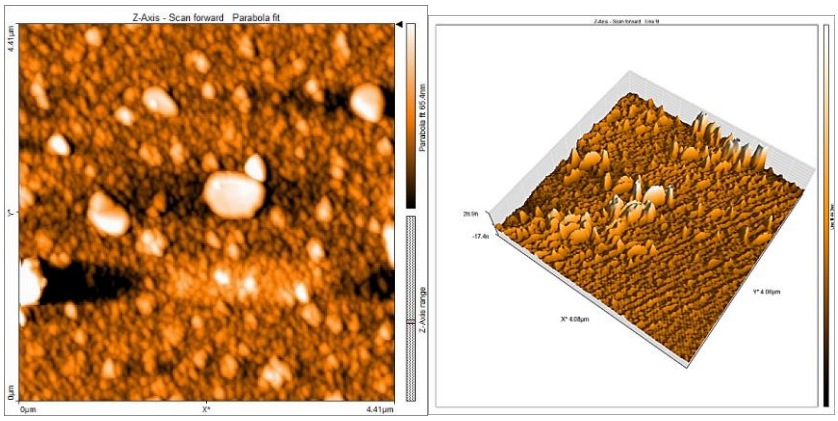

S-filter (As): None			
F: None			
Height parameters			
Sq	11.19	nm	Root-mean-square height
Ssk	0.4963		Skewness
Sku	3.482		Kurtosis
Sp	47.44	nm	Maximum peak height
Sv	29.41	nm	Maximum pit depth
Sz	76.85	nm	Maximum height
Sa	8.851	nm	Arithmetic mean height

Information				
Method	Threshold detection			
Threshold 1	110.4	nm		
Number of particles	220			
Coverage	45.45	%		
Density	52255435	Particles/mm²		
Individual results				
Parameters	**Projected Area**	**Area**	**Mean diameter**	**Z-maxim...**
Unit		nm²	nm	nm
Particle #1	Small	1449	39.97	115.3
Particle #2	Small	10432	94.96	139.4
Particle #3	Medium	60181	187.9	144.4
Particle #4	Small	141.3	10.56	116.0
Particle #5	Small	2254	49.03	127.3
Particle #6	Small	708.2	25.65	129.4
Particle #7	Small	4378	72.34	125.1
Particle #8	Small	16635	128.2	137.8
Global statistics				
Mean	*****	8765	68.92	129.3
Min	*****	18.21	2.982	110.4
Max	*****	78032	339.7	158.0

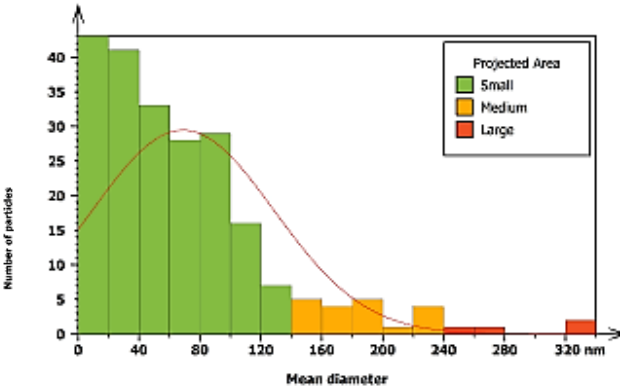

Figure 9. Morphology of poly(pyrrole-co-*p*-toluidine) film during polymerization on SS316L together with the average diameter and Root Mean Square Roughness (RMS) observed by atomic force microscopy.

3.6. X-Ray diffraction (XRD) analysis

X-Ray diffraction is employed to analyze the crystallographic structure of the materials. The X-ray diffraction analyses for poly(pyrrole-co-*p*-toluidine) are displayed in Figure 10. The XRD spectrum of the poly(pyrrole-co-*p*-toluidine) copolymer (1:1) ratio shows the sharp peaks at 2θ = 17.9°, 23.6°, and 2θ = 26.3°, revealing that the polymer shows semicrystalline behaviour [32].

Using Debye–Scherrer's approximation Equation 7 [33], we calculated the full width at half maximum (FWHM) of the peaks to determine the crystallite size of the sample.

$$d = k\lambda / \beta \cos\theta \tag{7}$$

where *d* represents the size of the crystallite, λ represents the wavelength radiation (λ = 1.542 Å), β represents the FWHM (in radians) of the diffraction peak in question, θ represents the diffraction angle, and *k* refers to the broadening constant (*k* = 0.91). The average size of the crystallites was detected to be 26.257 nm for poly(pyrrole-co-*p*-toluidine).

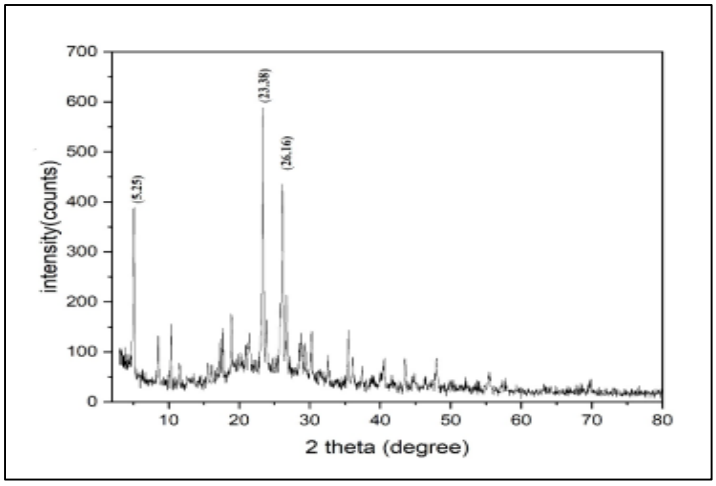

Figure 10. X-ray diffractions of poly(pyrrole- co-*p*-toluidine) coating on SS316L.

3.7. Field emission scanning electron microscopy (FESEM)

FESEM, or field emission scanning electron microscopy, was used to directly study the morphology of the synthesized poly(pyrrole-co-*p*-toluidine). The FESEM images of the bulk copolymer powder are shown in Figure 11. The surface of poly(pyrrole-co-*p*-toluidine) was covered of uniform size. Therefore, it can be inferred that this uniformly distributed partial copolymer can provide excellent protection for the substrate in corrosion tests. The synthesized copolymer films were obvious to have a structure that differed much from the cauliflower-like structure of polypyrrole as reported in the literature [34, 35]. Generally, *p*-toluidine has fibrillar and granular structure and poly pyrrole has a cauliflower-like structure as known according to the literature [34, 35]. The chemically synthesized copolymer shows the most similar morphology to the literature.

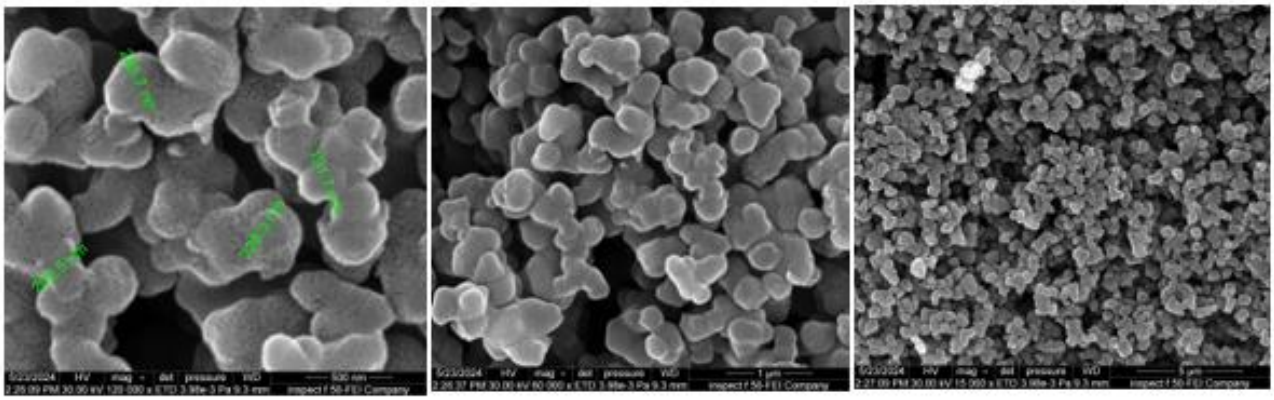

Figure 11. FE-SEM images for poly(pyrrole-co-*p*-toluidine) showing a spherical shape with particle size around 215 nm.

Conclusions

1. Based on the aforementioned findings, poly(pyrrole-co-*p*-toluidine) works well as a corrosion inhibitor in the saline medium.
2. Both the uncoated SS316 L and the alloy coated with poly(pyrrole-co-*p*-toluidine) in a 3.5% NaCl media corrode more quickly as the temperature rises. At 298 K, the inhibition effectiveness was reported to be as high as 98%.
3. Thermodynamics analysis reveals that as temperature rises, the coated SS316L ΔG values decrease with the rise of temperature. The coated samples exhibit positive ΔS values, suggesting a reduction in irregularity throughout the transition from reactants to the activated complex. The ΔH values exhibit endothermic behavior.
4. Energy-dispersive X-Ray spectroscopy (EDX) was used to analyze the surface composition and identify the presence of uniform size in poly(pyrrole-co-*p*-toluidine) using scanning electron microscopy (SEM) images. Based on these results, it can be concluded that this uniformly distributed partial copolymer can offer superior protection. Furthermore, when SS316 L was coated, its surface roughness was reduced, creating a smoother, more flexible surface. AFM verified this by displaying a uniform distribution and a homogenous exterior with spherical particles of regular size.
5. The thermal characteristics examined using the DSC equipment to guarantee product uniformity demonstrated a two-step weight loss process: the chemically manufactured copolymer was shown to lose weight at 240.80°C, while the removal of anions from the polymer structure is shown at 130.47°C.

References

1. W.D. Callister and D.G. Rethwisch, *Materials Science and Engineering: An Introduction*, New York, Wiley, 2018, p. 992.
2. G.F. Hays, *Corrosion Costs and the Future*, Link

3. M. Angelopoulos, Conducting Polymers in Microelectronics, *IBM Journal of Research and Development*, 2001, **45**, 57–75. doi: 10.1147/rd.451.0057
4. S. Cosnier, Recent Advances in Biological Sensors Based on Electrogenerated Polymers: A Review, *Anal. Lett.*, 2007, **40**, 1260–1279. doi: 10.1080/00032710701326643
5. K. Gurunathan, A.V. Murugan, R. Marimuthu, U.P. Mulik and D.P. Amalnerkar, Electrochemically Synthesized Conducting Polymeric Materials for Applications Towards Technology in Electronics, Optoelectronics and Energy Storage Devices, *Mater. Chem. Phys*., 1999, **61**, 173–191. doi: 10.1016/S0254-0584(99)00081-4
6. C.K. Chiang, C. Fincher, Y.W. Park, A.J. Heeger, H. Shirakawa, E.J. Louis, S.C. Gau, and A.G. MacDiarmid, Electrical conductivity in doped polyacetylene, *Phys. Rev. Lett*., 1977, **39**, no. 17, 1098. doi: 10.1103/Phys revlett39.1098
7. H. Shirakawa, E.J. Louis, A.G. MacDiarmid, C.K. Chiang and A.J. Heeger, Synthesis of electrically conducting organic polymers: halogen derivatives of polyacetylene, (CH)*x*, *J. Chem. Soc*., *Chem. Commun*., 1977, **16**, 578–580. doi: 10.1039/c3977000057
8. H. Shirakawa, The discovery of polyacetylene film: the dawning of an era of conducting polymers (Nobel lecture), *Angew. Chem. Int. Ed*., 2001, **40**, no. 14, 2574–2580. doi: 10.1002/1521-3773(20010716)40:14
9. H. Shirakawa, A. McDiarmid and A. Heeger, Twenty-five years of conducting polymers, *Chem. Commun*., 2003, **1**, 1–4. doi: 10.1039/b210718j
10. A.J. Heeger, Semiconducting, and metallic polymers: the fourth generation of polymeric materials (Nobel lecture), *Angew. Chem. Int. Ed*., 2001, **40**, no. 14, 2591–2611. doi: 10.1002/1521-3773(20010716)40:14
11. A.G. MacDiarmid, Synthetic metals: a novel role for organic polymers, *Synth. Met*., 2001, **125**, no. 1, 11–22. doi: 10.1016/S0379-6779(01)00508-2
12. A.G. MacDiarmid, Synthetic metals: A novel role for organic polymers (Nobel lecture), *Angew. Chem. Int. Ed*., 2001, **40**, no. 14, 2581–2590. doi: 10.1002/1521-3773(20010716)40:14
13. T.A. Skotheim and J.Reynolds, *Handbook of Conducting Polymers, 2 Volume Set*, Boca Raton, CRC press, 2007, p 1680. doi: 10.1201/b12346
14. R. Ravichandran, S. Sundarrajan, J.R. Venugopal, Sh. Mukherjee and S. Ramakrishna, Applications of conducting polymers and their issues in biomedical engineering, *J. R. Soc. Interface*, 2010, **7**, S559–S579. doi: 10.1098/rsif.2010.0120.focus
15. D.L. Wise, G.E. Wnek, D.J. Trantolo, T.M. Cooper and J.D.Gresser, *Electrical and Optical Polymer Systems: Fundamentals, Methods and Applicati*on, Boca Raton, CRC Press, 1998, p 1256. doi: doi:10.1201/9781482269888
16. D.E. Tallman, G. Spinks, A. Dominis and G.G. Wallace, Electroactive conducting polymers for corrosion control Part 1: General introduction and a review of non-ferrous metals, *Journal of Solid-State Electrochemistry*, 2002, **6**, 73–84, doi: 10.1007/s100080100212

17. N. Ahmad and A.G. MacDiarmid, Inhibition of corrosion of steels with the exploitation of conducting polymers, *Synth. Met.*, 1996, **78**, 103–110. doi: 10.1016/0379-6779(96)80109-3
18. T. Nelofar and M. Mobin, Corrosion Protection of Carbon Steel by Poly (aniline-co-o-toluidine) and Poly(pyrrole-co-o-toluidine) Copolymer Coatings, *J. Miner. Mater. Charact. Eng.*, 2011, **10**, no. 8, 735–753. doi: 10.4236/jmmce.2011.108058
19. X.G. Li, L.X. Wang, Y. Jin, Z.L. Zhu and Y.L. Yang, Preparation and identification of a soluble copolymer from pyrrole and *o*-toluidine, *J. Appl. Polym. Sci.*, 2001, **82**, 510–518. doi: 10.1002/app.1877
20. A.M. Alqudsi and K.A. Saleh, Conducting Polyanethole /Metals Oxides Nanocomposites for Corrosion Protection and Bioactivity, Baghdad Science Journal, 2024, **21**, no. 4, 1243–1254. doi: 10.21123/bsj.2023.8458
21. J. O'M. Bokris and A.K.N. Reddy, *Modern Electrochemistry 2B - Electronics in chemistry, engineering, biology, and environmental science*, 2nd Edition, Kluwer Academic/Plenum Publishers, New York, 2000, p 2004.
22. M. Stern and A.L. Geary, Electrochemical Polarization, I. A Theoretical Analysis of the Shape of Polarization Curves, *J. Electrochem. Soc.*, 1957, **104**, 56. doi: 10.1149/1.2428496
23. J.R. Santos, L.H. Mattoso and A.J. Motheo, Investigation of corrosion protection of steel by polyaniline films, *Electrochim. Acta*, 1998, **43**, 309–313. doi: 10.1016/S0013-4686(97)00052-2
24. C. Jeyaprabha, S. Sahiyanarayanan and G.V. Chari, Effect of cerium ions on corrosion inhibition of PANI for iron in 0.5 M H_2SO_4, *Appl. Surf. Sci.*, 2006, **253**, no. 2, 432–438. doi: 10.1016/j.opsusc.2005.12.081
25. M. Norzila and SI. Anis, Thermodynamic Study of Corrosion Inhibition of Mild Steel in Corrosive Medium by Piper nigrum Extract, *Indian J. Sci. Technol.*, 2015, **8**, no. 17, 1–7. doi: 10.17485/ijst/2015/v8i17/63478
26. R.A. Jassim, M.S. and A.M. Farhan, Protection of galvanized steel from corrosion in salt media using sulfur nanoparticles, *Baghdad Science Journal*, 2022, **19**, no. 2, 347–354. doi: 10.21123/bsj.2022.19.2.0347
27. E.G. Ogoke, SA. Odoemelam, BI.Eddy and N.O. Eddy, Adsorption and inhibitive properties of clarithromycin for the corrosion of zinc in 0.01 to 0.05M H2SO4, *Port. Electrohim. Acta*, 2009, **27**, 713–724. doi: 10.4152/pea.200906713
28. R.A. Jassim, K. Nafeesa, M. Halah and A.M. Farhan, Effect of Orphenadrine Citrate Drug on Corrosion of 316L Stainless Steel in Hydrochloric Acid, *Iraqi J. Sci.*, 2022, **63**, no. 7, 2793–2803. doi: 10.24996/ijs.2022.63.7.4
29. A. Zarrouk, B. Hammouti, H. Zarrok, R. Salghi, A. Dafali, Lh. Bazzi, L. Bammou and S.S. Al-Deyab, Electrochemical impedance spectroscopy and weight loss study for new pyridazine derivative as an inhibitor for copper in nitric acid, *Der Pharm. Chem.*, 2012, **4**, 337–346.

30. O. L. Riggs and R.M. Hurd, Temperature coefficient of corrosion inhibition, Corrosion, 1976, **23**, 252–260.
31. S.S. Gursoy, S. Cogal and A.U. Oksuz, Influence of surfactants on properties of electrochemically synthesized pyrrole/1- dimethylaminopyrrole copolymer, *Iran Polym. J.*, 2014, **23**, 783–792. doi: 10.1007/s13726-014-0274-3
32. V. Ponnuswamy, P. Jayamurugan and S. Deivanayaki, Synthesis and characterization of homo and poly(pyrrole-Co-O-Toluidine) copolymers to develop a charge transport material for solar cell applications, *J. Optoelectron. Adv. Mater*., 2010, **12**, no. 2, 315–320.
33. P. Giri, D. Goswami and A. Perumal, Advanced Nanomaterials and Nanotechnology, *Proceedings of the 2nd International Conference on advanced nanomaterials and nanotechnology*, 2013. doi: 10.1007/978-3-642-34216-5
34. A. Bibi and A. Shakoor, Charge transport mechanism in dodecyl benzenesulfonic acid doped polyaniline/carbon black composites, *Polym. Polym. Compos*., 2021, **29**, no. 9S, S1044–S1051. doi: 10.1177/09673911211040376
35. V.Q. Trung, T.H. Hanh, T.H. Quang, H.M. Hung, D.K. Linh, H.T. TuyetLan and L.M. Duc, Corrosion protection of molybdate doped polypyrrole film prepared in succinic acid solution, *Corros. Eng., Sci. Technol*., 2018, **53**, no. 1, 59–66. doi: 10.1080/1478422X.2017.1389370
36. V. Krishnakumar and R. Ramasamy, Vibrational spectra and structure of 5, 6-diamino uracil and 5, 6-dihydro-5-methyl uracil by density functional theory calculations, *Spectrochim. Acta, Part A*, 2007, **66**, 503–511. doi: 10.1016/j.saa.2006.02.066
37. S. Gunasekaran, S. Seshadri, S. Muthu, S. Kumaresan and R. Arunbalaji, Vibrational spectroscopy investigation using ab initio and density functional theory on p-anisaldehyde, *Spectrochim. Acta, Part A*, 2008, **70**, 550–556. doi: 10.1016/j.saa.2007.07.050
38. V. Krishnakumar, K. Parasuraman and A. Natarajan, A. Normal Coordinate Analysis of 5,6-dimethyl benzimidazole and Assignments of Infrared and Raman Bands, *Indian J. Pure. Appl. Phys*., 1997, **35**, 1–4.
39. X.G. Li, M.R. Huang, L.X. Wang, M.F. Zhu, A. Menner and J. Menner, Synthesis and characterization of pyrrole and mtoluidine copolymers, *Synth. Met*., 2001, **123**, 435–441. doi: 10.1016/S0379-6779(01)00317-4

♦ ♦ ♦